

PAPER • OPEN ACCESS

## Synthesis of anisotropic Au–Cu alloy nanostructures and its application in SERS for detection of methylene blue

To cite this article: Manish Kumar Singh *et al* 2020 *Mater. Res. Express* **7** 015052

View the [article online](#) for updates and enhancements.



**IOP | ebooks™**

Bringing together innovative digital publishing with leading authors from the global scientific community.

Start exploring the collection—download the first chapter of every title for free.



## PAPER


## Synthesis of anisotropic Au–Cu alloy nanostructures and its application in SERS for detection of methylene blue

## OPEN ACCESS

RECEIVED  
28 October 2019REVISED  
5 December 2019ACCEPTED FOR PUBLICATION  
19 December 2019PUBLISHED  
13 January 2020

Original content from this work may be used under the terms of the [Creative Commons Attribution 4.0 licence](#).

Any further distribution of this work must maintain attribution to the author(s) and the title of the work, journal citation and DOI.

Manish Kumar Singh<sup>1,3,4</sup> , Prajwal Chettri<sup>2</sup>, Joysurya Basu<sup>1</sup>, Ajay Tripathi<sup>2</sup>, Bratindranath Mukherjee<sup>1</sup>, Archana Tiwari<sup>2</sup> and R K Mandal<sup>1</sup><sup>1</sup> Department of Metallurgical Engineering, Indian Institute of Technology (BHU), Varanasi-221005, Uttar Pradesh, India<sup>2</sup> Department of Physics, School of Physical Sciences, Sikkim University, Gangtok-737102, Sikkim, India<sup>3</sup> Current Address: Department of Materials Science and Engineering, University of Connecticut, Storrs, CT-06269, USA<sup>4</sup> Author to whom any correspondence should be addressed.E-mail: [manish.singh@uconn.edu](mailto:manish.singh@uconn.edu) and [drmanishsg@gmail.com](mailto:drmanishsg@gmail.com)**Keywords:** multiply twinned, nanowires, oriented attachment, localized surface plasmon resonance, surface enhanced Raman scatteringSupplementary material for this article is available [online](#)**Abstract**

Au–Cu alloy nanostructures have been synthesized in aqueous phase through co-reduction of  $\text{HAuCl}_4 \cdot 3\text{H}_2\text{O}$  and  $\text{CuCl}_2 \cdot 2\text{H}_2\text{O}$  by glucose in presence of hexadecylamine at  $\sim 80^\circ\text{C}$ . By changing the synthesis conditions, nanostructures of various shapes such as nanowires, multiply twinned tripod, tetrapod, etc were observed. Systematic variation of the synthesis condition not only leads to change in size and particle morphology but also develops various other crystallographic characters in the nanoparticles. Alloying behavior of Au–Cu has been examined through transmission electron microscope operating in its conventional and analytical modes coupled with high resolution phase contrast microscopy. These results suggested that nanostructures are composed of homogeneous Au–Cu alloy. Preferential attachment along  $\{111\}$  and  $\{100\}$  crystallographic facets of Au–Cu alloy nanoparticles led to the formation of nanowires. Multiply twinned branched shape Au–Cu (width of branch  $\sim 30$  nm) nanostructures exhibit localized surface plasmon resonance maxima in the near-infrared region. The branched shape Au–Cu alloy nanostructures display better surface enhanced Raman scattering response in the detection of methylene blue as compared to spherical Au nanoparticles.

**1. Introduction**

The simultaneous control of morphology and composition of bimetallic nanoparticles (NPs) is complicated by two processes in wet chemical synthesis. They refer to nature of nucleation and growth of two metals precursors concurrently. Metals pair possess large difference in the redox potentials quite often making co-reduction a difficult route for synthesis of alloy nanoparticles. However, synthesis of bimetallic/ alloy NPs of noble metals (Au, Cu and Ag) helps to modulate localized surface plasmon resonance (LSPR) spectral response compared to monometallic NPs making use of their synergy. Spherical gold NPs, for example, can possess a plasmon band typically ranging from 520 nm to the infra-red regime depending on the particle size and shape [1, 2]. The Copper NPs (Cu NPs) have been attractive for their ability to catalyze chemical reactions [3]. Additionally, Cu possesses a surface plasmon resonance (SPR) which can impart unique optical properties that can be exploited for sensing, imaging, and photonics applications. Unfortunately, one limitation of Cu is that it rapidly oxidizes to form  $\text{CuO}$  and  $\text{Cu}_2\text{O}$ , and therefore the synthesis of Cu NPs is challenging compared to those of Ag and Au NPs. However, Cu is observed to be stable for prolonged period in the presence of Ag at nanometer length scale [4]. The optical properties of gold NPs have also been modified by alloying the particle with another metal [5]. The resulting plasmon band behaves as a hybrid of the two materials, and possesses variability based upon the proportion incorporated. This ability to tune material properties via composition combined with the wide variety of shapes available makes gold NPs an important candidate for investigations both in elemental as well as in alloy form. Literature on the synthesis of controlled morphology and composition of Au–Cu bimetallic NPs is

scarce [6–8]. Liu and Walker synthesized Au–Cu alloy nanocubes employing a polyol method [7]. They showed that the size and composition of the nanocubes influenced the localized surface plasmon resonance (LSPR) behavior significantly. Chen *et al* grew intermetallic Au–Cu NPs by allowing Cu atoms to diffuse into pre-synthesized Au seeds [6]. Structural modifications in Au–Cu nanostructures at local level have also been observed by heat-treatments of nonstoichiometric AuCu alloy nanoparticles in solution as well as in solid state phases [9, 10]. Solution phase synthesis gives uniform and monodispersed products owing to homogeneous atomic scale diffusion compared to that of solid-state diffusion. In spite of some remarkable studies reported in the literature, well-defined and controlled morphology of Au–Cu bimetallic NPs are still elusive. Moreover, NPs were reported to expose high symmetric facets such as {111} {100} and {110} very often [11]. Control of nature of the crystal structure, exposed surfaces and facets of NPs directly dictates their properties. There is a continuous push for the synthesis of nanostructures with various interesting shapes including those of NPs with multiple branches. Nanostructures with anisotropic features such as branches, corners, edges, and bends are expected to give increased high energy sites vis-à-vis of isotropic ones. They can be used to manipulate LSPR spectral response, as SERS (surface enhanced Raman scattering) substrates as well as catalysts [12–15]. It has been shown in the literature that branched nanostructures are often exhibited vicinal surfaces decorated with low symmetric facets [16–19]. These surfaces possess many crystallographic defects which can serve as potential sites for chemical reactions to take place [14, 17–19]. Limited reports are available pertaining to the synthesis of alloy NPs with multiple branches. This work attempts to synthesize branched shape Au–Cu alloy NPs and study their LSPR and SERS behaviors. This investigation proposes to address formation of another interesting morphology of technological importance related to nanowires. It has been shown that there are two main mechanisms by which anisotropic shapes evolve in the growth process. They are referred to as classical Ostwald ripening (OR) and oriented attachment (OA) mechanisms [20]. It has also been deliberated in the literature that the formation of NPs is a consequence of the growth of stable clusters by attachment of adatoms. [21–25]. A more direct study towards this end has been carried out through *in situ* transmission electron microscopy (TEM) [20]. One of the important findings of this study was to establish the formation of NPs through the growth of pre-formed clusters [26]. Further, NPs can attach themselves crystallographically and formed nanowires which are commonly known as oriented attachment in the literature [20, 27–31]. In a typical liquid phase chemical synthesis, the NPs formation is the result of the growth of initially formed seeds. The seed is the stable aggregates of adatoms produced by the reduction of precursors. Growth of NPs are usually restricted by stabilizers and NPs move randomly in liquid phase. It has been reported that when two NPs approaches each other, the formation of anisotropic structures is a consequence of the nature of stabilizers and strength of van der Waals forces acting between them [28]. The purpose of this communication is to synthesize Au–Cu alloy nanostructures with varied morphologies by changing the reaction conditions such as molar ratio of stabilizer and precursors. We describe herein a facile and rapid method utilizing low temperature to synthesize Au–Cu nanostructures in aqueous medium through wet chemical route. It will also be demonstrated that presence of Cu-ions is necessary to initiate anisotropy in nanostructures. In addition, mechanistic studies pertaining to growth of Au–Cu alloy nanowires has also been discussed in the light of kinetically controlled oriented attachment of particles. The manipulation of LSPR spectral response from visible to near infrared region associated with shape of Au–Cu nanostructures (nanopods) has been observed. The SERS activity of Au–Cu alloy nanopods has been investigated to detect methylene blue molecule and results are compared to that of pure Au NPs. Attempts have been made to correlate the SERS results with observed morphologies and LSPR behavior. We have chosen methylene blue (MB) as a probe molecule for examining the SERS activity of Au–Cu alloy nanopods and Au-NPs as MB is widely used dye by textile, dying and pharmaceutical industries. MB is a heterocyclic aromatic compound and due to its strong hydrophilic nature, it can easily contaminate water bodies in the form of effluents which poses hazard to the environment due to its toxic and non-biodegradable nature [32, 33].

## 2. Material and methods

### 2.1. Synthesis of Au–Cu nanostructures

Forty-five mg of hexadecylamine (HDA) was mixed in 4.0 ml of deionized water with the help of ultra-sonicator for about 1.0 h till complete mixing. In this emulsion, 0.3 ml (0.1 M)  $\text{CuCl}_2 \cdot 2\text{H}_2\text{O}$  and 0.3 ml (0.1 M)  $\text{HAuCl}_4 \cdot 3\text{H}_2\text{O}$  was added and stirred magnetically for 10 min at room temperature. A light green color solution was observed. This solution was placed in an oil bath maintained at  $\sim 80^\circ\text{C}$  for about 15 min and a light blue color appears within several minutes. At this point 0.3 ml (1.0 M) freshly prepared glucose solution was added in hot condition and capped the vial. After 2–3 min, the blue color changed to light purple and within a few minutes transformed into black color. The reaction was continued for 10 min. The vial was taken out from the oil bath and cooled to room temperature. This alloy will be referred to as A0911 from here onwards, where first two digits show HDA concentration in mg/ml and the next two digits correspond to precursors molar ratio

**Table 1.** Alloy designation and associated synthesis conditions such as stabilizer concentration and precursors molar ratio. Growth morphology observed through TEM and UV-vis absorbance peaks are also given.

Alloy designation	HDA concentration (mg/ml)	Precursors molar ratio Au: Cu	Morphology observed (TEM)	UV-vis absorbance peak (nm)
A0910	9	1:0	quasi-spherical	520
A0911	9	1:1	multipods	~520 and ~800
A1811	18	1:1	nanowires	—
A2711	27	1:1	nanowires	—
A3611	36	1:1	nanowires	—
A1831	18	3:1	nanowires	—
A1821	18	2:1	multipods	~ 520 and ~ 800
A1812	18	1:2	nanowires	—

(Au: Cu). Details of synthesis conditions and corresponding alloy designation are given in table 1. The samples were cleaned by repeated addition of n-hexane and ethanol followed by centrifugation and ultrasonication. The powder thus obtained was dispersed in n-hexane and a drop was coated on a TEM grid (carbon coated Ni-grid with mesh size 400). The morphology and structures have been investigated by TEM (FEI Tecnai G<sup>2</sup> T20, operating at 200 kV). The average chemistry of the grown nanostructures was assessed by high angle annular dark field—scanning TEM—x-ray energy dispersive spectroscopy (HAADF-STEM-EDS). UV-vis spectrometer (Agilent Cary UV-vis and Perkin-Elmer Lambda XLS+) was utilized to investigate the LSPR behavior of the sols.

## 2.2. Preparation of SERS substrates

The method to prepare SERS substrate and parameters used in Raman measurements is given in detail elsewhere [15]. In brief, Au and Au–Cu nanopowders were added in MB solution with a concentration of 1  $\mu\text{M}$ . This mixture was thoroughly mixed through ultrasonication and suspension obtained was aged for 24 h. At last, the suspension was drop cast on a silicon substrate and was dried before SERS investigations.

## 3. Results and discussion

### 3.1. Effect of HDA concentration on Au–Cu growth morphology

Growth morphology was followed by varying the concentration of stabilizer ( $\sim 9 \text{ mg ml}^{-1}$ ,  $18 \text{ mg ml}^{-1}$ ,  $27 \text{ mg ml}^{-1}$ , and  $36 \text{ mg ml}^{-1}$ ) keeping other reaction parameters nearly the same. Figure 1(a) displays branched Au–Cu nanostructures of sample A0911. The appearance of bipod, tripod and tetrapod nanostructures were seen. In A1811, A2711, and A3611 wire-like features associated with many nodes and stems have been observed. For example, in A1811 (HDA concentration  $\sim 18 \text{ mg ml}^{-1}$ ) nanowires with average width,  $\sim 6.0 \text{ nm}$  and length  $\sim 90 \text{ nm}$  have been observed. The selected area diffraction patterns for both branched (A0911) and wires (A1811) nanostructures are shown in figures 2(a) and (b) respectively. The rings could be indexed systematically, and phase was found to be those of FCC solid solution of AuCu. The possible mechanism for the formation of multipods can be explained in the following way. At the beginning of reaction ions of Au and Cu reduced to Au and Cu by glucose. The Au ions will get reduced first due to higher redox potential (1.002 V) compared to that of Cu ions (0.34 V).

This leads to a large population of small seed crystals. The sub-nanometer size particles containing multiply twinned crystallographic defects viz., icosahedra and decahedra have been reported to be stable than cuboctahedra [11, 34–36]. This leads to the formation of multiply twinned seeds. The concentration of Au-ions in the suspension went down very fast due to their faster reduction, whereas Cu-ions concentration was maintained at a relatively high level. The multiply twinned particles grown initially could not be sustained further and subsequent growth seems to be controlled by kinetics. Adatoms attached preferentially at twinning planes owing to high energy sites rather on facets. This preferential deposition could be attributed to the underpotential deposition of Cu on Au seeds [37]. The twin boundaries observed in tripod and tetrapod nanostructures are shown in figure S1 (supplementary information is available online at [stacks.iop.org/MRX/7/015052/mmedia](https://stacks.iop.org/MRX/7/015052/mmedia)). The preferential attachments of metal atoms along the twinning planes of multiply twinned seeds led to the formation of multipods. The chemistry of the Au–Cu multipods was investigated by HAADF-STEM-EDS and average composition was found to be  $\sim 80 \text{ at\% Au}$  and  $\sim 20 \text{ at\% Cu}$  respectively. The STEM-EDS elemental maps shown in figure 3 depicted uniform distribution of Au and Cu throughout the tripod and tetrapod features. It was inferred that Au–Cu alloy has been formed. In order to probe the influence of Cu ions in the formation of multipods, an experiment was conducted without Cu precursor (referred to as A0910 in table 1). The morphology and corresponding SAD pattern are presented in figures 4(a) and (b)

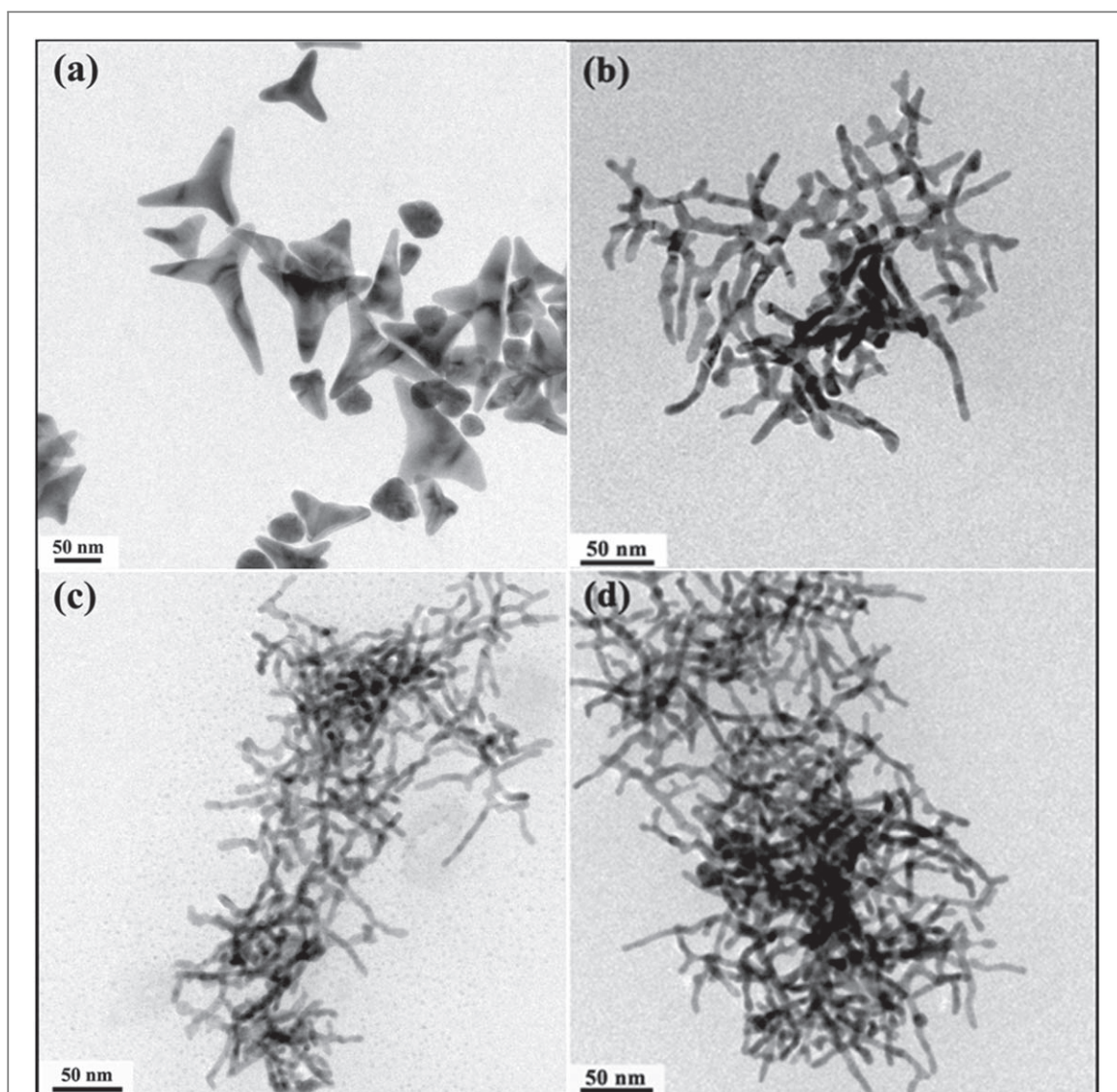


Figure 1. Growth morphology of Au–Cu nanostructures of (a) A0911, (b) A1811, (c) A2711, and (d) A3611 respectively.

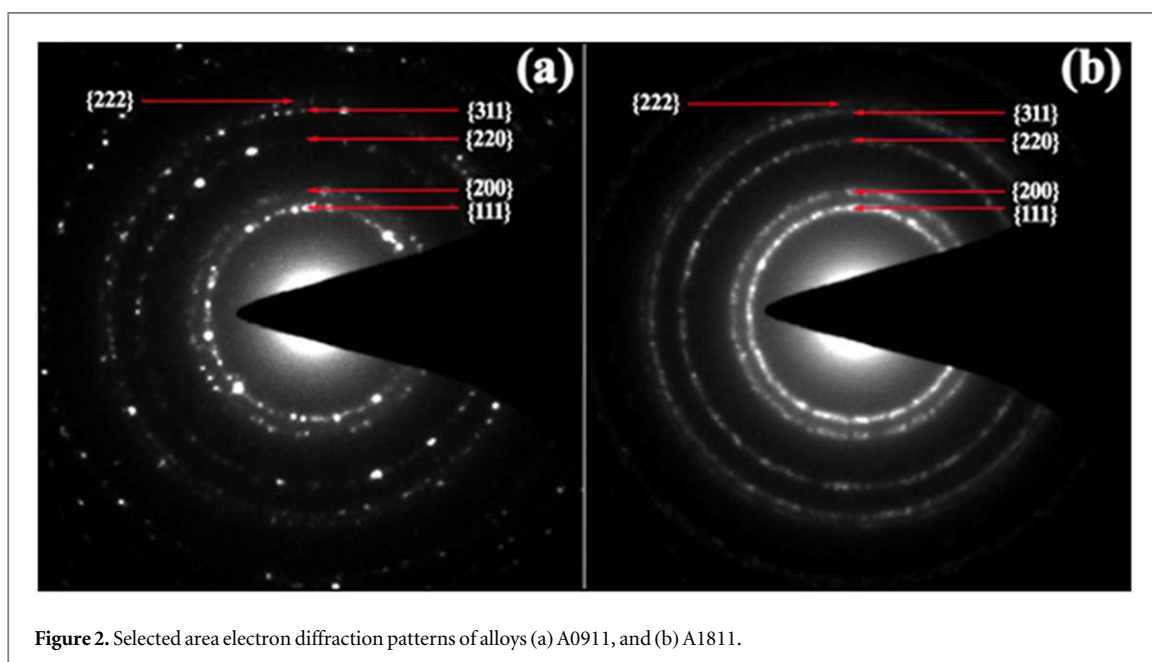
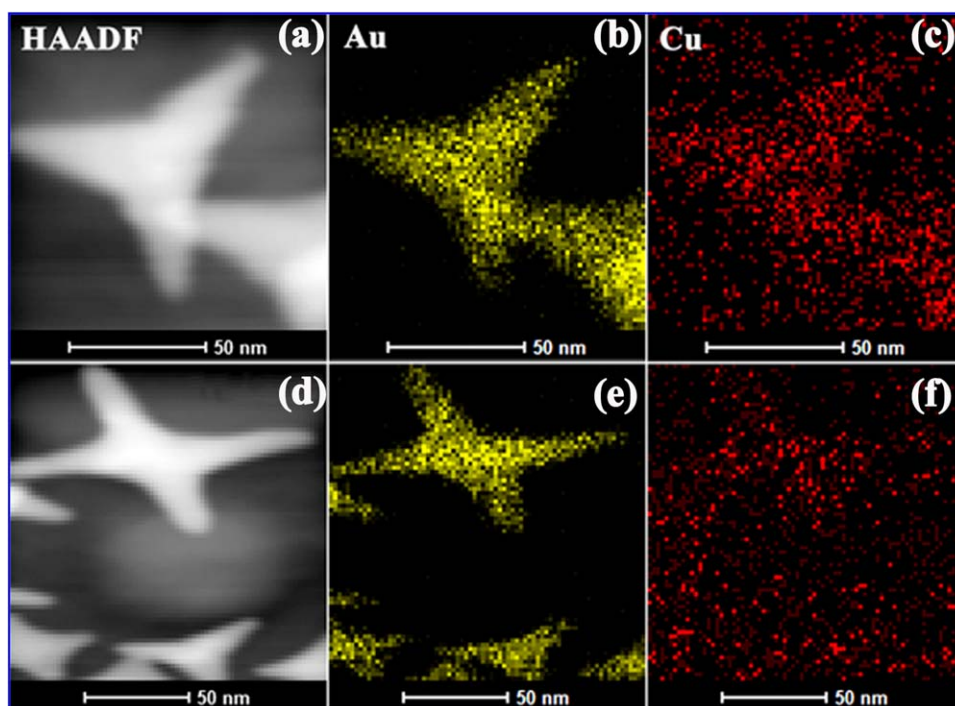
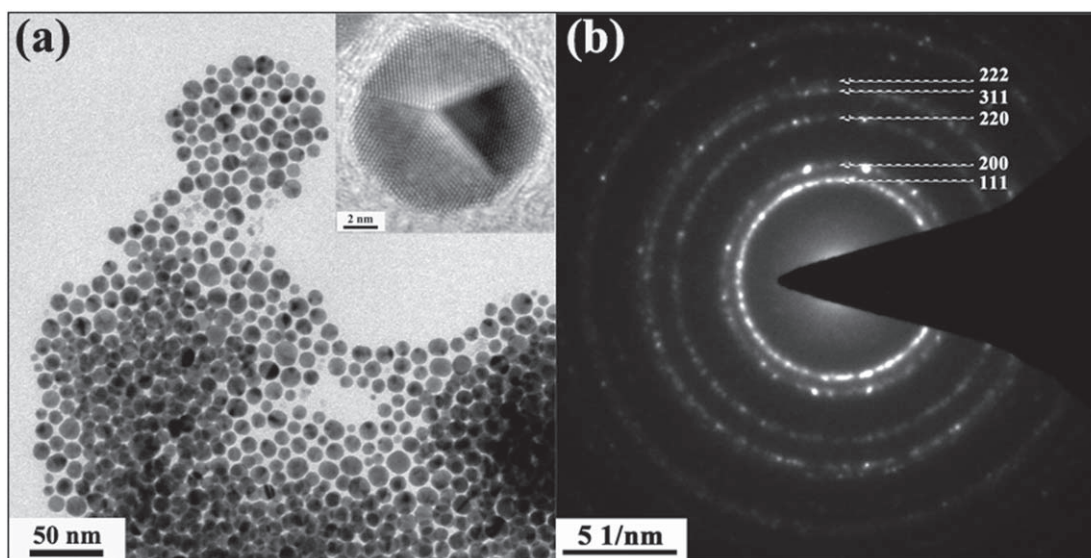


Figure 2. Selected area electron diffraction patterns of alloys (a) A0911, and (b) A1811.



**Figure 3.** STEM-EDS elemental maps of a tripod (a) HAADF image, (b) Au map, (c) Cu map and a tetrapod (d) HAADF image, (e) Au map, and (f) Cu map in alloy A0911.



**Figure 4.** (a) TEM image of A0910 with a high-resolution phase contrast image as an inset showing twin boundary and (b) indexed rings corresponding to the image shown in (a).

respectively. A HRTEM image of a particle shown as an inset in figure 4(a) displays twins. The TEM image shows that nearly spherical NPs of average size  $\sim 8.0$  nm have formed. The DP was indexed, and phase was found to those of FCC-Au. The absence of morphological anisotropy points out that the presence of Cu ions seems to play a substantial role in promoting the anisotropy in Au–Cu nanostructures in the present synthesis conditions.

### 3.2. Effect of precursors ratio on Au–Cu growth morphology

The experiments were also designed to investigate the role of precursors molar ratio (Au: Cu) on the growth morphology of the nanostructures while keeping the HDA concentration  $\sim 18$  mg ml $^{-1}$ . Figure 5 depicts images showing morphology with changing precursor molar ratios of Au: Cu as 3:1, 2:1, 1:1 and 1:2 respectively (A1831, A1821, A1811, and A1812). The wire-like features with nodes and stems have been observed in all the samples

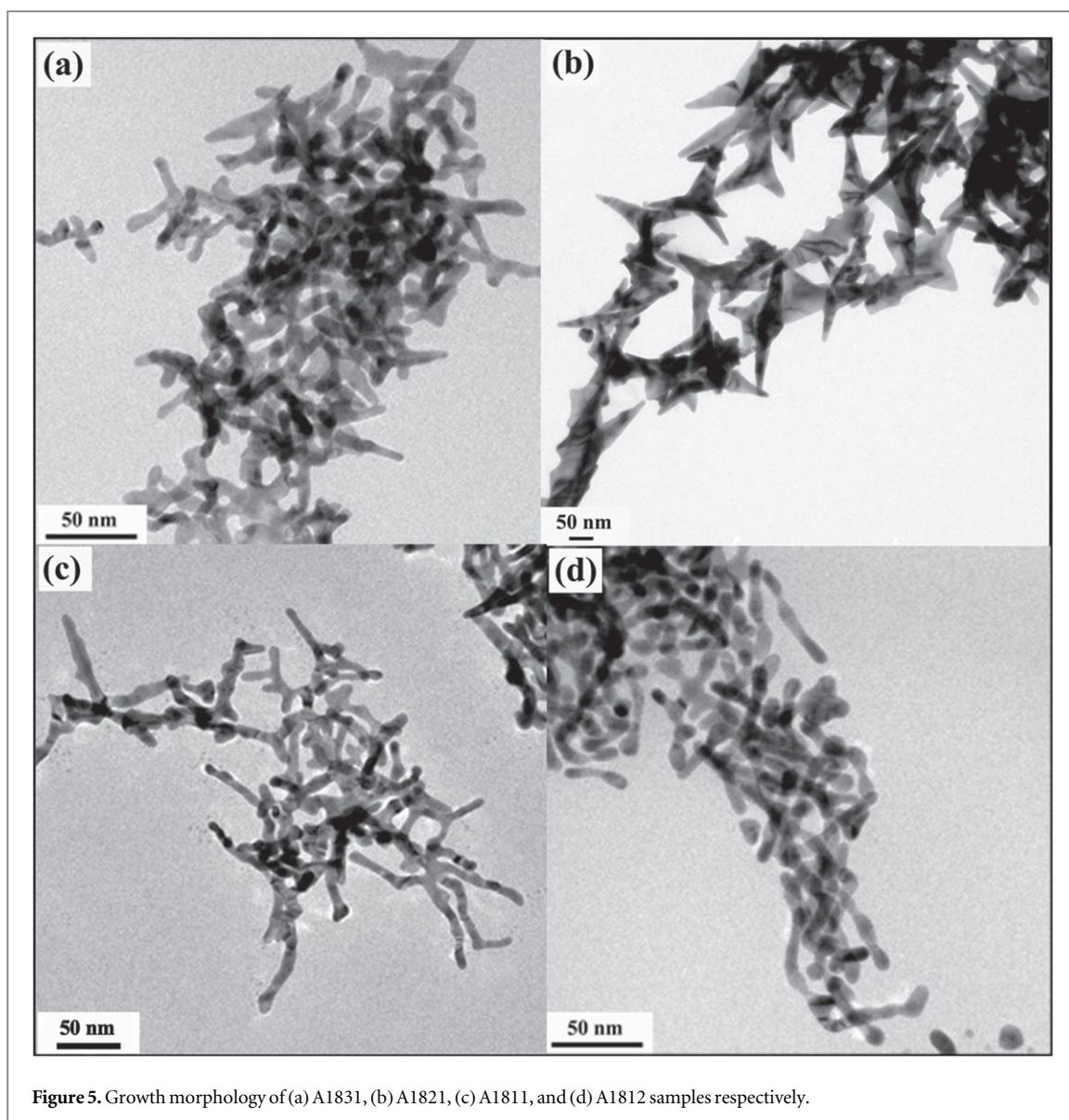


**Figure 5.** Growth morphology of (a) A1831, (b) A1821, (c) A1811, and (d) A1812 samples respectively.

except A1821 where AuCu multipods were observed. The SAD patterns in all the cases could be indexed to those of FCC-AuCu (shown in figure S2, supplementary information). Based on the above observations, it may be argued that the ratio of Au precursor with HDA play an important role in the formation of AuCu multipods. The ratio of  $\text{HAuCl}_4 \cdot 3\text{H}_2\text{O}$  to HDA for A0911 and A1821 is nearly the same and observation of multipods in them appears to be rather accommodating. The HAADF image and STEM-EDS spectrum of AuCu nanowires are displayed in figure S3 (supplementary information). The presence of both Au and Cu in nanowires indicating the formation of an AuCu alloy phase. The average composition of Au and Cu was found to be  $\sim 52$  at% and  $\sim 48$  at% respectively. The lattice parameter was derived to be  $\sim 3.85$  Å by invoking Vegard's law.

### 3.3. Formation of Au–Cu nanowires

The AuCu alloy nanowires was observed when experiments were conducted with molar precursors ratio and HDA concentration as Au: Cu (1:1) and  $\sim 18$  mg  $\text{ml}^{-1}$  onwards respectively. Interrupted growth experiments were carried out to decipher the growth mechanism of the AuCu nanowires. The aliquots were taken out after 2 min, 4 min, 6 min, and 10 min after addition of glucose from A1811 alloy. The evolution of growth morphology was followed with TEM investigations and images are shown in figure 6(a) to 6(d). In 2 min grown sample, nanowires with many nodes and stems having average width  $\sim 4$  nm and length of  $\sim 200$  nm were observed. In addition, NPs of the average size  $\sim 3$  nm were also observed. As the growth proceeds further, particle density decreased, and more nodes and stems emerged in 4 min grown sample. The average width and length were measured to be  $\sim 5$  nm and 100 nm respectively. The average particle size, in this case, was found to be  $\sim 5$  nm. In 6 min grown sample, the average width and length of the nanowires was observed to be  $\sim 7.0$  nm and 70 nm respectively and finally, after 10 min of growth, no significant change in the dimensions of the

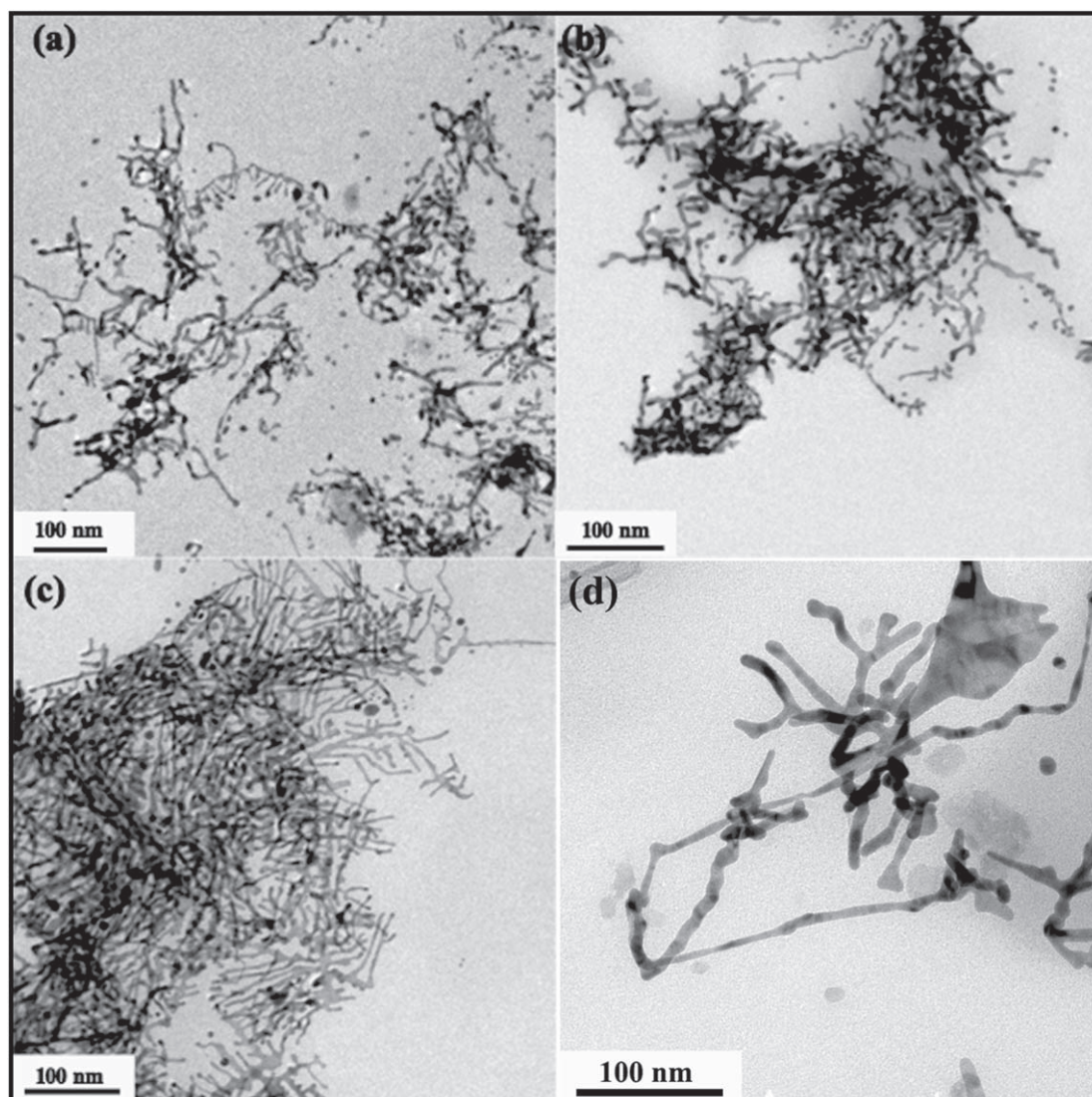


**Figure 6.** Temporal evolution of Au–Cu morphology of A1811 at (a) 2 min, (b) 4 min, (c) 6 min, and (d) 10 min respectively.

nanowires was noticed. The co-existence of nanowires and larger size of the NPs suggest that both OR and OA mechanisms (mentioned in section 1) are operative in the present synthesis conditions during the growth process. To investigate the insight of the formation of nanowires and branched morphologies, HRTEM images were acquired from two minutes grown sample of Au–Cu nanostructures and is shown in figure 7. Figure 7(a) displays defect-free single crystalline NWs oriented along  $\langle 111 \rangle$  direction with lattice fringe spacing of  $\sim 0.21$  nm corresponding to d-spacing of  $\{111\}$  planes of FCC AuCu. It may be attributed to perfect matching of the particles along  $\{111\}$  planes as observed in the case of Au nanowires [28]. Figure 7(b) shows attachment of three crystals along via twin boundaries. The exposed facet planes of crystal 1 are observed to be  $\{111\}$  and  $\{100\}$ , expected from FCC crystal. Crystals 1,2 and 2,3 are found to be attaching along  $\{111\}$  planes through twin. The attachment of two particles along  $\{100\}$  planes are depicted in figure 7(c), however, a misorientation of less than  $1^\circ$  have been noticed in this case. Figure 7(d) shows HRTEM image from Au–Cu branched nanostructure displaying exposed facets mostly of  $\{111\}$  types. Additionally, planar faults such as twins are also seen. Our findings suggest that initially formed Au–Cu NPs attached themselves along  $\{111\}$  planes perfectly or through twins giving rise to anisotropic morphology. Moreover, particles exhibit low energy facets of the types  $\{111\}$  and  $\{100\}$ , can also undergo aforesaid crystallographic attachment process and led to the branched morphology. This growth mode appears to be different than those reported in the literature for nanowire [38–40]. For instance, twin defects in the Ag seeds were reported to be crucial for the formation of Ag nanowires [40]. On contrary to this, defects were not essentially required for the formation of Au and Pt–Ag nanowires [26, 28].



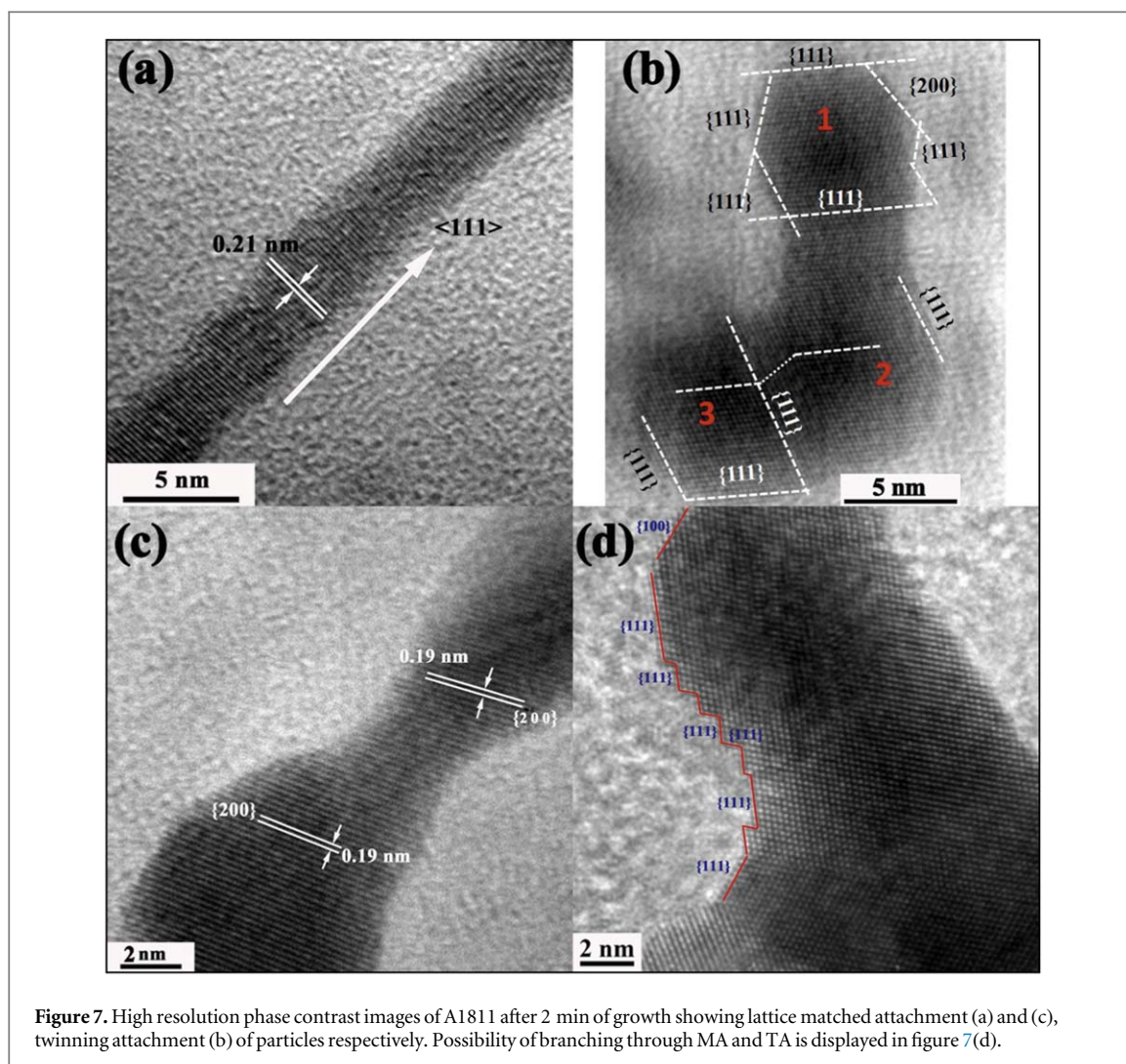


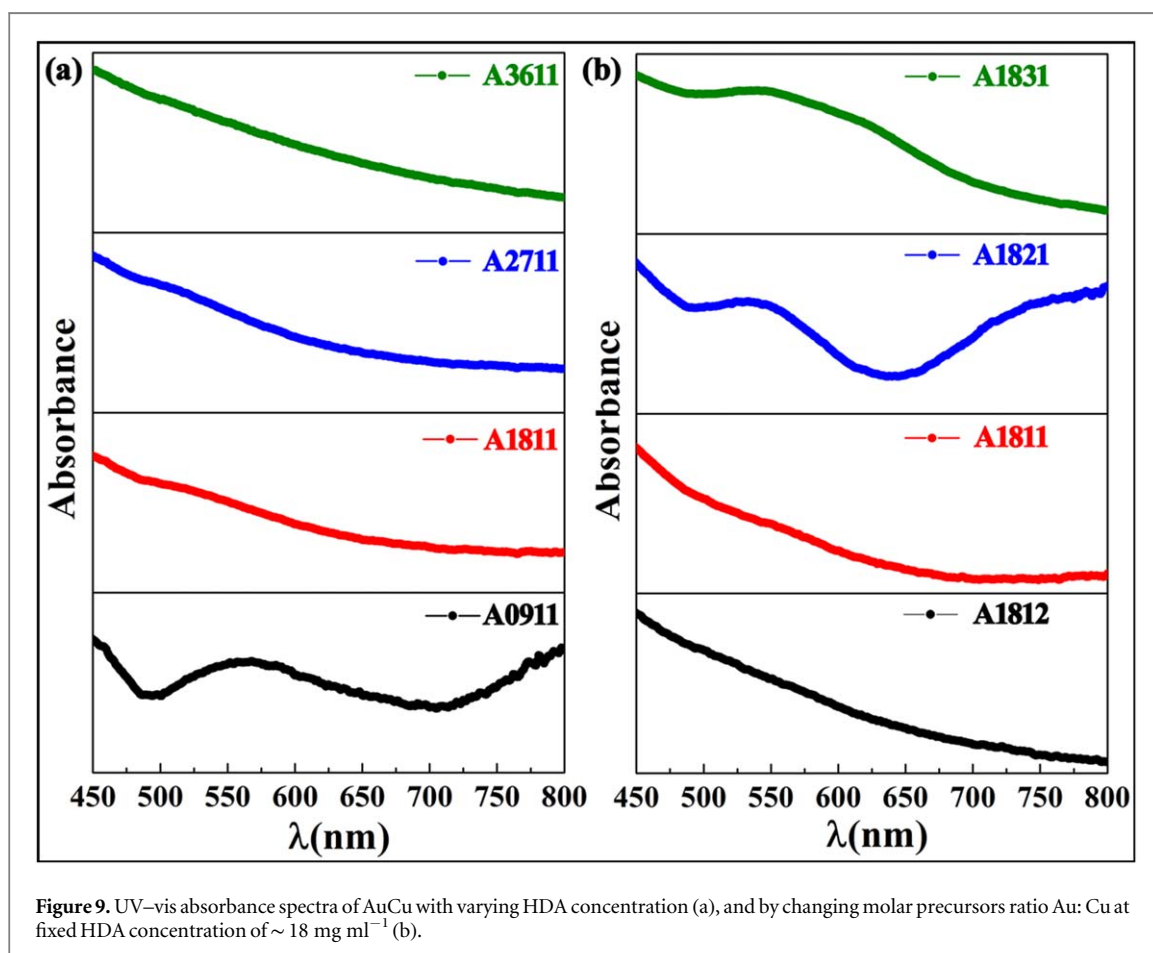
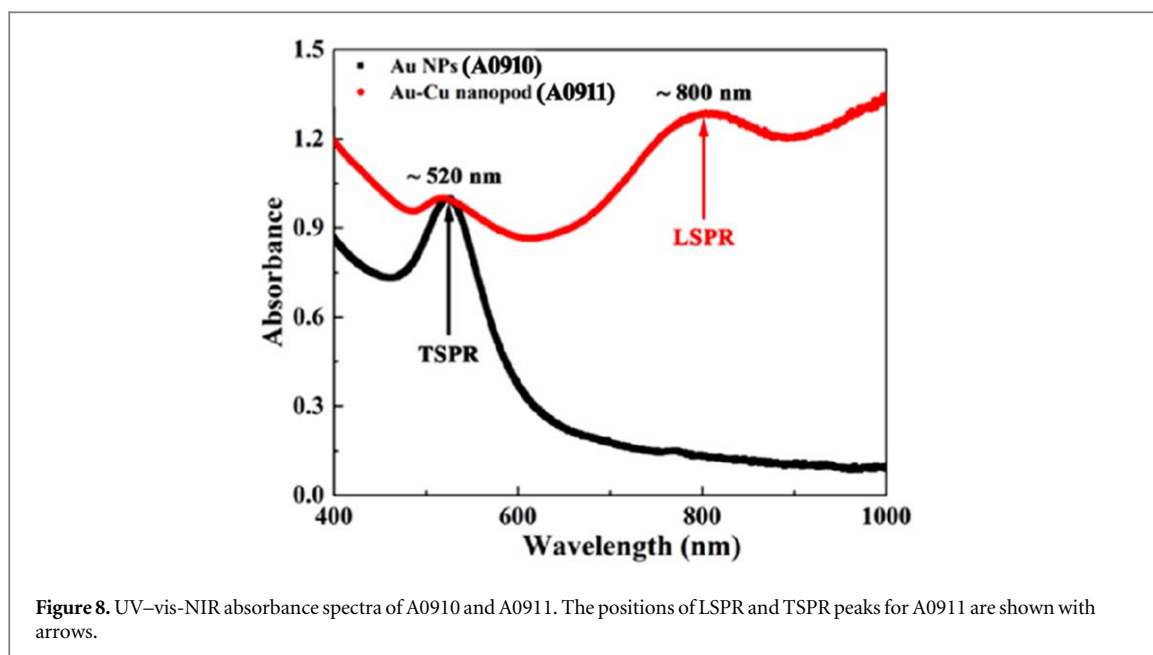
**Figure 7.** High resolution phase contrast images of A1811 after 2 min of growth showing lattice matched attachment (a) and (c), twinning attachment (b) of particles respectively. Possibility of branching through MA and TA is displayed in figure 7(d).

### 3.4. LSPR behavior of Au–Cu alloy nanostructures

The UV–vis–NIR absorbance spectra (200 nm–1100 nm) of A0910 and A0911 is shown in figure 8. The LSPR absorbance maxima  $\lambda_{\max}$  corresponding to A0910 is observed at  $\sim 520$  nm. The LSPR response of A0911 shows the presence of a peak in the visible region at  $\sim 520$  nm and a peak in near infra-red region at  $\sim 800$  nm. This drastic red shift in the LSPR peak can be attributed to excitation of higher order multipoles [11]. When the concentration of HDA was increased from  $\sim 9$  mg ml $^{-1}$  to  $\sim 18$  mg ml $^{-1}$  and onwards, no LSPR peak was observed (cf figure 9(a)). As discussed in section 3.1, morphologies observed from TEM are wire-like for A1811, A2711, and A3611 respectively. The highly agglomerated nanowires might lead to absence of LSPR peak in 200 nm to 800 nm range. The appearance of LSPR response similar to A0911 has been observed for A1821 as displayed in figure 9(b). The LSPR peaks in near infra-red region motivated us to conduct SERS measurements with a source excitation wavelength of 785 nm as discussed in the following section.

### 3.5. SERS study of Au NPs and Au–Cu alloy Nanopods

In order to investigate the SERS activity of Au NPs and Au–Cu multipods (A0910, A0911 and A1821), methylene blue (MB) was chosen as a probe molecule. For comparison, normal Raman spectrum of MB powder was collected using 0.003 mW of the laser power as shown in figure 10(A). The Raman peaks for MB appear at 1622 cm $^{-1}$  (ring stretching of C–C), 1500 cm $^{-1}$  (asymmetrical stretching of C–C), 1441 cm $^{-1}$  (asymmetrical stretching of C–N), 1395 cm $^{-1}$  (symmetrical stretching of C–N), 1300 cm $^{-1}$  (in-plane ring deformation of C–H), 1180 cm $^{-1}$  (stretching of C–N), 1155–771 cm $^{-1}$  (in-plane bending of C–H), 591 cm $^{-1}$  (skeletal deformation of C–S–C) and 501 cm $^{-1}$ –448 cm $^{-1}$  (skeletal deformation of C–N–C) [33]. Figure 10(B) (a) shows normal Raman spectrum of 100  $\mu$ M MB using a bare Si substrate. It is evident that due to the low concentration of MB used only fewer Raman vibrational signatures of MB are visible as compared to MB powder (cf figure 10(A)). The SERS response of A0910, A0911 and A1821 are investigated by lowering the concentration of MB to 1  $\mu$ M as shown in figure 10(B) (b), (c) and (d) respectively. It is apparent that A0910 does not show Raman vibrational signatures of



MB in the entire scan range except a peak appearing at  $521 \text{ cm}^{-1}$  which is the background signal from Si substrate. In contrast to previous findings where Au NPs are known to be SERS active, we attribute the absence of SERS effect in A0910 to two major factors: first, as can be seen from the TEM images (cf figure 4(a)) that the Au NPs are spherical and mono-dispersed with no tell-tale signs of agglomeration. The SERS activity of metal NPs are mainly contributed by the presence of rough surfaces and edges in nanoparticle as well as NPs clusters which act as hotspots for the enhancement of Raman signal [41, 42]. The synthesized Au NP in this work lacks all of these features which manifests itself into a SERS inactive substrate at a concentration of  $1 \mu\text{M}$  of MB. Second, for

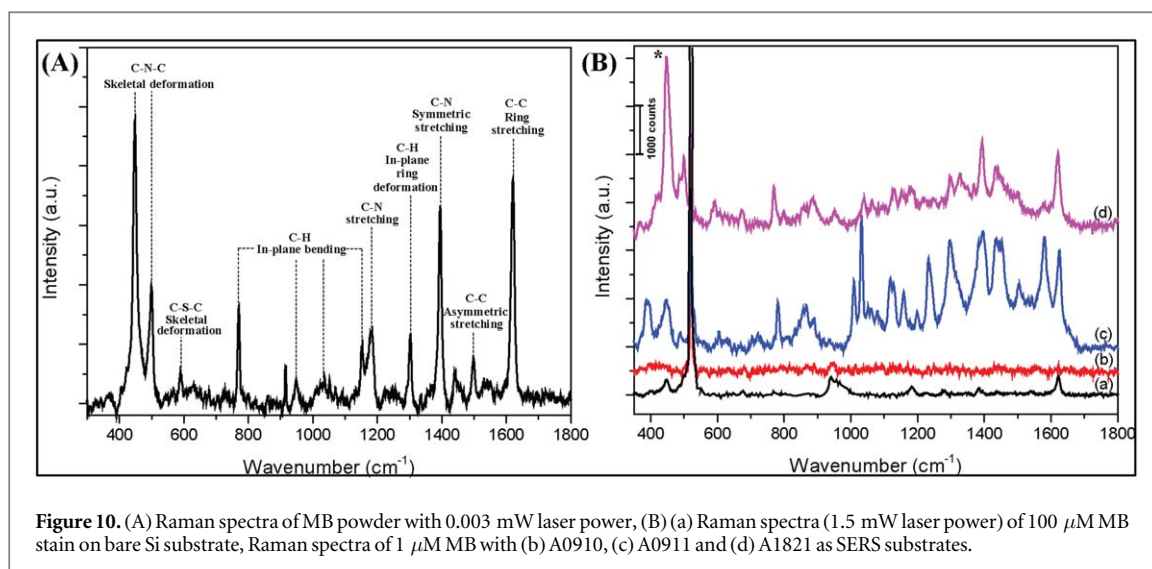


**Figure 10.** (A) Raman spectra of MB powder with 0.003 mW laser power, (B) (a) Raman spectra (1.5 mW laser power) of 100  $\mu\text{M}$  MB stain on bare Si substrate, Raman spectra of 1  $\mu\text{M}$  MB with (b) A0910, (c) A0911 and (d) A1821 as SERS substrates.

maximum SERS enhancement, the laser excitation wavelength should be close to the plasmon resonance frequency of NPs [43, 44]. The UV–vis–NIR absorbance spectrum of A0910 (cf figure 9) shows the  $\lambda_{\text{max}}$  lies at  $\sim 520$  nm which is in the far energy range as compared to the laser excitation energy (785 nm). However, in case of A0911 and A1821, strong Raman vibrational signatures of MB (1  $\mu\text{M}$ ) appear which is either weak or absent while using bare Si as a substrate (100  $\mu\text{M}$  MB). This observation suggests that they act as potential SERS substrate for detecting MB. The alloys A0911 and A1821 have similar multiply twinned branched shape morphology with sharp edges and corners that allows for the strong coupling of laser electromagnetic field leading to enhancement of MB signal via SERS effect [41, 42, 44]. Additionally, these samples show an additional LSPR peak centred at  $\lambda_{\text{max}} \sim 800$  nm as discussed in UV–vis section (cf see figure 9). As the SERS spectra are collected with 785 nm excitation wavelength which is very close to LSPR  $\lambda_{\text{max}} \sim 800$  nm, we attribute the facilitation of electromagnetic enhancement of Raman signal due to activation of LSPR at 785 nm which leads to generation of electromagnetic field in the vicinity of the NP via which the MB molecule interacts leading to enhancement of its Raman signal [43, 44]. Furthermore, the branched shaped nanostructures in A0911 and A1821 also possess a higher surface to volume ratio as compared to spherical Au NPs (A0910) leading to increased adsorption capacity for MB molecules over its surface. The excess presence of MB molecule over branched nanostructures also contributes to enhancing the SERS signal.

In addition to the observed SERS effect in A0911 and A1821, the SERS spectra of MB differ in peak profile as compared to that of normal Raman spectrum of MB powder (cf figure 10(A)). The appearance of peaks at  $1580\text{ cm}^{-1}$ ,  $1230\text{ cm}^{-1}$ ,  $1120\text{ cm}^{-1}$ ,  $1038\text{ cm}^{-1}$ ,  $1011\text{ cm}^{-1}$  and  $863\text{ cm}^{-1}$  using A0911 as a SERS substrate are either weak or not visible in normal Raman spectrum of MB powder. Similarly, peaks at  $1329\text{ cm}^{-1}$  and  $888\text{ cm}^{-1}$  in case of alloy A1821 are absent/feeble in normal Raman spectrum of MB powder. By comparing figure 10(B) (c) and (d) a peculiar trend in the relative increase in the intensity of Raman peaks of MB can be observed. For instance, the peaks at  $448\text{ cm}^{-1}$  and  $501\text{ cm}^{-1}$  for alloy A0911 (figure 10(B) (c)) are relatively weaker in intensity as compared to the intensity of peaks lying between  $1011\text{--}1622\text{ cm}^{-1}$  and vice-versa for the alloy A1821. The enhancement in the intensity depends on the orientation of the MB molecule with respect to the NP surface. For MB molecule adsorbed with its plane parallel to the surface of NPs, out of plane bending mode will be more enhanced and vice-versa compared to its orientation perpendicular to NP surface [44]. In addition to that, the peaks appearing at  $1300\text{ cm}^{-1}$ ,  $1395\text{ cm}^{-1}$ ,  $1441\text{ cm}^{-1}$ ,  $1500\text{ cm}^{-1}$ , and  $1580\text{ cm}^{-1}$  are considerably enhanced when A0911 is used as a SERS substrate as compared to that of A1821. Although there is a nearly similar increase in the intensity of Raman peaks of MB with A0911 and A1821 as SERS substrates, the drastic increase in intensity in some of these peaks in A0911 as compared to that in A1821 suggests interplay of chemical enhancement in addition to electromagnetic enhancement contributing to SERS. This suggests that charge transfer from A0911 to MB is more pronounced compared to that of A1821 which is due to a drastic difference of surface energies leading to charge transfer from high energy branched nanostructures to MB [44, 45]. The enhancement in the Raman peak intensity of MB using Au and Au–Cu alloy nanostructures as SERS substrates can be quantified in terms of enhancement factor (EF) defined as  $EF = I_{\text{SERS}} C_{\text{NRS}} / I_{\text{NRS}} C_{\text{SERS}}$ , where  $I_{\text{SERS}}$  is the Raman peak intensity of MB molecule with concentration  $C_{\text{SERS}}$  while using A0910, A0911 and A1821 as SERS substrates and  $I_{\text{NRS}}$  is the normal Raman peak intensity of MB molecule having concentration  $C_{\text{NRS}}$  while using Si as a substrate. The peak highlighted by \* ( $448\text{ cm}^{-1}$ ) in figure 10(B) has been chosen as a reference peak for calculating EF as it is a well distinguished and enhanced as compared to other

peaks. Due to SERS inactive A0910 substrate, no peak corresponding to MB appears (figure 10(B)(b)) and hence the EF of A0911 and A1821 have been calculated. The obtained value of EF corresponding to A1821 substrate is far more superior ( $EF = 1.2 \times 10^3$ ) as compared to that of A0911 ( $EF = 3.2 \times 10^2$ ). The sharp increase of EF in A1821 may be attributed to the increased concentration of Au contributing to SERS in Au–Cu alloy nanostructure as compared to A0911.

## 4. Conclusions

It has been shown that manipulation of the morphology of AuCu alloy nanostructures by varying reaction conditions such as concentrations of stabilizer and molar ratio of precursors at  $\sim 80^\circ\text{C}$  is possible. Extensive electron microscopy investigation revealed the development of various crystallographic characters during the growth of the nanostructures as well as their alloying behavior. The presence of Cu-ions is capable of incubating anisotropy in the grown nanostructures through changing the surface/interface energies of initially formed nanocrystals. The HDA concentration of  $\sim 9\text{ mg ml}^{-1}$  gave rise to branched Au–Cu alloy NPs. The ratio of Au-precursor to HDA appears to play an important role in the growth of branched Au–Cu alloy NPs. With further increase in the concentration of HDA ( $\sim 18\text{ mg ml}^{-1}$  onwards) nanowires have been observed with several branch and bends. The formation of nanowires under the present synthesis conditions has been explained in terms of oriented attachment kinetics of AuCu alloy NPs. Multiply twinned branched shape AuCu alloy (width of branch  $\sim 30\text{ nm}$ ) products display strong LSPR peak in the near-infra-red region ( $\sim 800\text{ nm}$ ). These nanostructures employed as a SERS substrate for detection of MB and their response has been observed superior to that of pure spherical Au NPs. This study may serve as a template to modulate the LSPR behavior by controlling the shape and composition for other alloy systems.

## ORCID iDs

Manish Kumar Singh  <https://orcid.org/0000-0001-5004-7809>

## References

- [1] Singh M K, Mukherjee B and Mandal R K 2017 Growth morphology and special diffraction characteristics of multifaceted gold nanoparticles *Micron* **94** 46–52
- [2] Eustis S and El-Sayed M A 2006 Why gold nanoparticles are more precious than pretty gold: noble metal surface plasmon resonance and its enhancement of the radiative and nonradiative properties of nanocrystals of different shapes *Chem. Soc. Rev.* **35** 209–17
- [3] Soomro R A, Sherazi S H, Memon N, Shah M, Kalwar N, Hallam K R and Shah A 2014 Synthesis of air stable copper nanoparticles and their use in catalysis *Advanced Materials Letters* **5** 191–8
- [4] Singh M K, Manda P, Singh A and Mandal R 2015 Localized surface plasmon behavior of Ag–Cu alloy nanoparticles stabilized by rice-starch and gelatin *AIP Adv.* **5** 107108
- [5] Kim M-J, Na H-J, Lee K C, Yoo E A and Lee M 2003 Preparation and characterization of Au–Ag and Au–Cu alloy nanoparticles in chloroform *J. Mater. Chem.* **13** 1789–92
- [6] Chen W, Yu R, Li L, Wang A, Peng Q and Li Y 2010 A seed-based diffusion route to monodisperse intermetallic CuAu nanocrystals *Angew. Chem. Int. Ed.* **49** 2917–21
- [7] Liu Y and Walker A H 2010 Monodisperse gold–copper bimetallic nanocubes: facile one-step synthesis with controllable size and composition *Angew. Chem. Int. Ed.* **49** 6781–5
- [8] Yin F, Wang Z W and Palmer R E 2011 Controlled formation of mass-selected Cu–Au core–shell cluster beams *J. Am. Chem. Soc.* **133** 10325–7
- [9] Singh M K, Basu J, Mukherjee B and Mandal R 2019 Determination of symmetry breaking transitions and polymorphism in AuCu nanostructures by nano-beam electron diffraction *Mater. Charact.* **54** 437–48
- [10] Singh M K, Mukherjee B, Basu J and Mandal R 2018 Vacancy-mediated structural changes in Au–Cu nanoparticles *Philos. Mag. Lett.* **98** 97–106
- [11] He R, Wang Y-C, Wang X, Wang Z, Liu G, Zhou W, Wen L, Li Q, Wang X and Chen X 2014 Facile synthesis of pentacle gold–copper alloy nanocrystals and their plasmonic and catalytic properties *Nat. Commun.* **5** 4327
- [12] Liao H G, Jiang Y X, Zhou Z Y, Chen S P and Sun S G 2008 Shape-controlled synthesis of gold nanoparticles in deep eutectic solvents for studies of structure–functionality relationships in electrocatalysis *Angew. Chem. Int. Ed.* **47** 9100–3
- [13] Zhang H, Xia X, Li W, Zeng J, Dai Y, Yang D and Xia Y 2010 Facile synthesis of five-fold twinned, starfish-like rhodium nanocrystals by eliminating oxidative etching with a chloride-free precursor *Angew. Chem.* **122** 5424–8
- [14] Zhang L F, Zhong S L and Xu A W 2013 Highly branched concave Au/Pd bimetallic nanocrystals with superior electrocatalytic activity and highly efficient SERS enhancement *Angew. Chem. Int. Ed.* **52** 645–9
- [15] Singh M K, Chettri P, Basu J, Tripathi A, Mukherjee B, Tiwari A and Mandal R 2019 Synthesis of rod-shaped Au–Cu intermetallic nanoparticles and SERS detection *Mater. Lett.* **249** 33–6
- [16] Quan Z, Wang Y and Fang J 2012 High-index faceted noble metal nanocrystals *Acc. Chem. Res.* **46** 191–202
- [17] Wang F, Li C, Sun L-D, Wu H, Ming T, Wang J, Yu J C and Yan C-H 2010 Heteroepitaxial growth of high-index-faceted palladium nanoshells and their catalytic performance *J. Am. Chem. Soc.* **133** 1106–11
- [18] Zhang J, Langille M R, Personick M L, Zhang K, Li S and Mirkin C A 2010 Concave cubic gold nanocrystals with high-index facets *J. Am. Chem. Soc.* **132** 14012–4
- [19] Zhang L, Niu W and Xu G 2012 Synthesis and applications of noble metal nanocrystals with high-energy facets *Nano Today* **7** 586–605

- [20] Banfield J F, Welch S A, Zhang H, Ebert T T and Penn R L 2000 Aggregation-based crystal growth and microstructure development in natural iron oxyhydroxide biomineralization products *Science* **289** 751–4
- [21] Park J, Joo J, Kwon S G, Jang Y and Hyeon T 2007 Synthesis of monodisperse spherical nanocrystals *Angew. Chem. Int. Ed.* **46** 4630–60
- [22] Peng Z and Yang H 2009 Designer platinum nanoparticles: control of shape, composition in alloy, nanostructure and electrocatalytic property *Nano Today* **4** 143–64
- [23] Tao A R, Habas S and Yang P 2008 Shape control of colloidal metal nanocrystals *small* **4** 310–25
- [24] Xia Y, Xiong Y, Lim B and Skrabalak S E 2009 Shape-controlled synthesis of metal nanocrystals: simple chemistry meets complex physics? *Angew. Chem. Int. Ed.* **48** 60–103
- [25] Yin Y and Alivisatos A P 2004 Colloidal nanocrystal synthesis and the organic–inorganic interface *Nature* **437** 664
- [26] Peng Z, You H and Yang H 2010 Composition-dependent formation of platinum silver nanowires *ACS nano* **4** 1501–10
- [27] Cademartiri L and Ozin G A 2009 Ultrathin nanowires—a materials chemistry perspective *Adv. Mater.* **21** 1013–20
- [28] Halder A and Ravishanker N 2007 Ultrafine single-crystalline gold nanowire arrays by oriented attachment *Adv. Mater.* **19** 1854–8
- [29] Penn R L and Banfield J F 1998 Imperfect oriented attachment: dislocation generation in defect-free nanocrystals *Science* **281** 969–71
- [30] Tang Z and Kotov N A 2005 One-dimensional assemblies of nanoparticles: preparation, properties, and promise *Adv. Mater.* **17** 951–62
- [31] Zhang Q, Liu S-J and Yu S-H 2009 Recent advances in oriented attachment growth and synthesis of functional materials: concept, evidence, mechanism, and future *J. Mater. Chem.* **19** 191–207
- [32] Mellish K J, Cox R D, Vernon D I, Griffiths J and Brown S B 2002 *In vitro* photodynamic activity of a series of methylene blue analogues *Photochem. Photobiol.* **75** 392–7
- [33] Li C, Huang Y, Lai K, Rasco B A and Fan Y 2016 Analysis of trace methylene blue in fish muscles using ultra-sensitive surface-enhanced Raman spectroscopy *Food Control* **65** 99–105
- [34] Elechiguerra J L, Reyes-Gasga J and Yacamán M J 2006 The role of twinning in shape evolution of anisotropic noble metal nanostructures *J. Mater. Chem.* **16** 3906–19
- [35] Mayoral A, Barron H, Estrada-Salas R, Vazquez-Duran A and José-Yacamán M 2010 Nanoparticle stability from the nano to the meso interval *Nanoscale* **2** 335–42
- [36] Yacamán M J, Ascencio J, Liu H and Gardea-Torresdey J 2001 Structure shape and stability of nanometric sized particles *Journal of Vacuum Science & Technology B: Microelectronics and Nanometer Structures Processing, Measurement, and Phenomena* **19** 1091–103
- [37] Personick M L, Langille M R, Zhang J and Mirkin C A 2011 Shape control of gold nanoparticles by silver underpotential deposition *Nano Lett.* **11** 3394–8
- [38] Maksimuk S, Teng X and Yang H 2007 Roles of twin defects in the formation of platinum multipod nanocrystals *The Journal of Physical Chemistry C* **111** 14312–9
- [39] Teng X and Yang H 2005 Synthesis of platinum multipods: an induced anisotropic growth *Nano Lett.* **5** 885–91
- [40] Wiley B, Sun Y, Mayers B and Xia Y 2005 Shape-controlled synthesis of metal nanostructures: the case of silver *Chemistry—A European Journal* **11** 454–63
- [41] Darienzo R, Chen O, Sullivan M, Mironava T and Tannenbaum R 2018 Quasi-fractal gold nanoparticles for SERS: effect of nanoparticle morphology and concentration *ChemRxiv* (<https://doi.org/10.26434/chemrxiv.7482098.v1>)
- [42] Zhu S-Q, Zhang T, Guo X-L and Zhang X-Y 2014 Self-assembly of large-scale gold nanoparticle arrays and their application in SERS *Nanoscale Res. Lett.* **9** 114
- [43] Agrawal A, Kriegel I and Milliron D J 2015 Shape-dependent field enhancement and plasmon resonance of oxide nanocrystals *The Journal of Physical Chemistry C* **119** 6227–38
- [44] Smitha S, Gopchandran K, Ravindran T and Prasad V 2011 Gold nanorods with finely tunable longitudinal surface plasmon resonance as SERS substrates *Nanotechnology* **22** 265705
- [45] Wang T, Hu X and Dong S 2006 Surfactantless synthesis of multiple shapes of gold nanostructures and their shape-dependent SERS spectroscopy *The Journal of Physical Chemistry B* **110** 16930–6